Mg²⁺ regulation of kinase signaling and immune function

Chryssa Kanellopoulou[1,2]*, Alex B. George[1,2]*, Evan Masutani[1,2,3], Jennifer L. Cannons[1,4], Juan C. Ravell[1,2], Tori N. Yamamoto[5,6,7], Margery G. Smelkinson[8], Ping Du Jiang[1,2], Mami Matsuda-Lennikov[1,2], Julie Reilley[1,4], Robin Handon[4], Ping-Hsien Lee[5,6], J. Richard Miller[9], Nicholas P. Restifo[5,6], Lixin Zheng[1,2], Pamela L. Schwartzberg[1,4], Matthew Young[10], and Michael J. Lenardo[1,2]

Mg²⁺ is required at micromolar concentrations as a cofactor for ATP, enzymatic reactions, and other biological processes. We show that decreased extracellular Mg²⁺ reduced intracellular Mg²⁺ levels and impaired the Ca²⁺ flux, activation marker up-regulation, and proliferation after T cell receptor (TCR) stimulation. Reduced Mg²⁺ specifically impairs TCR signal transduction by IL-2–inducible T cell kinase (ITK) due to a requirement for a regulatory Mg²⁺ in the catalytic pocket of ITK. We also show that altered catalytic efficiency by millimolar changes in free basal Mg²⁺ is an unrecognized but conserved feature of other serine/threonine and tyrosine kinases, suggesting a Mg²⁺ regulatory paradigm of kinase function. Finally, a reduced serum Mg²⁺ concentration in mice causes an impaired CD8⁺ T cell response to influenza A virus infection, reduces T cell activation, and exacerbates morbidity. Thus, Mg²⁺ directly regulates the active site of specific kinases during T cell responses, and maintaining a high serum Mg²⁺ concentration is important for antiviral immunity in otherwise healthy animals.

Introduction

Mg²⁺ is required at micromolar concentrations as an essential cofactor for many fundamental biological processes, especially enzymatic reactions involving kinases, nucleic acids, and ATP (Weston, 2008; de Baaij et al., 2015). The typical American diet is insufficient in Mg²⁺, leading the US Dietary Guidelines Advisory Committee to classify Mg²⁺ as a shortfall nutrient of public health concern (Costello et al., 2016). Moreover, genetic variation, illnesses, and drugs can cause persistent reductions in serum Mg²⁺ (Tong and Rude, 2005; Meyer et al., 2010; Cundy and Mackay, 2011). Approximately 95% of intracellular Mg²⁺ is tightly bound with micromolar affinity as a counterion and cofactor to nucleic acids and nucleotides such as ATP, proteins, and other macromolecules. This "bound" Mg²⁺ is typically stable at a setpoint concentration between 10 and 20 mM depending on the cell type (de Baaij et al., 2015). By contrast, a small percentage (usually ~5% or 0.5–1 mM) is basal "free" Mg²⁺ that is unbound and chemically active and whose concentration, $[Mg^{2+}]_i$, can vary in the low-millimolar range. The free basal Mg²⁺ dynamically exchanges with free external Mg²⁺, $[Mg^{2+}]_e$, to establish an electrochemical equilibrium and is not buffered by the bound Mg²⁺ (MacDermott, 1990; Chaigne-Delalande et al., 2013). Patients with X-linked immunodeficiency with Mg²⁺ defect, Epstein–Barr virus, and neoplasia (XMEN) disease due to a loss of expression of Mg²⁺ transporter 1 (*MAGT1*) have impaired Mg²⁺ homeostasis, reduced $[Mg^{2+}]_i$, abnormal N-linked glycosylation, and defective immune responses (Zhou and Clapham, 2009; Cherepanova et al., 2014; Shrimal et al., 2015). How changes in $[Mg^{2+}]_i$ alter T cell receptor signaling and immune cell function is unknown.

Results

Mg²⁺ deprivation impairs T cell activation

To investigate T cell responses, we reduced the free basal $[Mg^{2+}]_i$ by varying the $[Mg^{2+}]_e$ (Chaigne-Delalande et al., 2013). In lymphocytes, we have determined that total Mg²⁺, $[Mg^{2+}]_T$, = 17 mM based on an assumed resting isotonic lymphocyte cell volume of 200 femtoliters (Deutsch and Lee, 1988; Li et al., 2011;

[1]Molecular Development of the Immune System Section, Laboratory of Immune System Biology, National Institute of Allergy and Infectious Diseases, National Institutes of Health, Bethesda, MD; [2]Clinical Genomics Program, National Institute of Allergy and Infectious Diseases, National Institutes of Health, Bethesda, MD; [3]Medical Scientist Training Program, School of Medicine, University of California, San Diego, San Diego, CA; [4]Genetic Disease Research Branch, National Human Genome Research Institute, Bethesda, MD; [5]Center for Cancer Research, National Cancer Institute, National Institutes of Health, Bethesda, MD; [6]Center for Cell-Based Therapy, National Cancer Institute, National Institutes of Health, Bethesda, MD; [7]Immunology Graduate Group, University of Pennsylvania, Philadelphia, PA; [8]Biological Imaging, Research Technology Branch, National Institute of Allergy and Infectious Diseases, National Institutes of Health, Bethesda, MD; [9]Early Discovery Pharmacology, Merck & Co., Boston, MA; [10]Department of Internal Medicine, University of Michigan Medical School, Ann Arbor, MI.

*C. Kanellopoulou and A.B. George contributed equally to this paper; Correspondence to Michael J. Lenardo: lenardo@nih.gov.

Chaigne-Delalande et al., 2013). To mimic the decreased $[Mg^{2+}]_i$ levels observed in XMEN patient T cells without other biochemical effects due to MagT1 gene deficiency (Chaigne-Delalande et al., 2013), we equilibrated T lymphocytes from healthy donors in different levels of $[Mg^{2+}]_e$ to achieve different free basal $[Mg^{2+}]_i$ using either Mg^{2+}-depleted medium (dRPMI), $[Mg^{2+}]_e$ <0.10 mM; reduced Mg^{2+} medium (rRPMI), $[Mg^{2+}]_e \approx 0.13 \pm 0.01$ mM; or complete medium (cRPMI), $[Mg^{2+}]_e \approx 0.59 \pm 0.04$ mM. To accurately quantitate $[Mg^{2+}]_i$, we adapted a null point titration assay developed by Flatman and Lew (1980) (Grynkiewcz et al., 1985; Ng et al., 1991). We initially used flow cytometry to measure the response of an internal probe in permeabilized cells exposed to various concentrations of $[Mg^{2+}]_e$ (Fig. 1 A) and the Grynkiewicz equation (Fig. 1 B; Grynkiewicz et al., 1985). We determined that cycling T cell blasts have a $[Mg^{2+}]_i = 0.54 \pm 0.18$ mM in cRPMI, 0.44 ± 0.19 mM in rRPMI, and 0.39 ± 0.1 mM in dRPMI. We confirmed these values using a standard cuvette-based fluorometric assay that allows more rapid equilibration (Fig. 1, B and C). We found this assay had excellent reproducibility between experiments and gave values of $[Mg^{2+}]_i$ in cRPMI = 0.77 mM $\pm$ 0.23 mM, rRPMI = 0.48 mM $\pm$ 0.07 mM, and dRPMI 0.31 mM $\pm$ 0.16 mM (Fig. 1 D). Because $[Mg^{2+}]_T$ in resting human lymphocytes is 17 mM (Chaigne-Delalande et al., 2013), these values for free basal $[Mg^{2+}]_i$ are between 1.7% and 4.5% of $[Mg^{2+}]_T$. Therefore, $[Mg^{2+}]_i$ can vary in the millimolar range in T lymphocytes from healthy donors depending on $[Mg^{2+}]_e$.

We next tested the responsiveness of T cells and found that the CD69 activation marker was significantly decreased in both CD4$^+$ and CD8$^+$ cells 18 h after TCR stimulation in dRPMI and rRPMI compared with cRPMI (Fig. 1, E–H). Similarly, CD25 was significantly reduced 36 h after activation in rRPMI and dRPMI (Fig. 1, E–H). The cell viability using these media ranged from 80–92% (Fig. S1, A and B). Importantly, the proliferation of both CD4$^+$ and CD8$^+$ cells was dramatically reduced when cells were activated and expanded in lower Mg^{2+} concentrations for five days (Fig. 1, I and J), with a decrease titrating from cRPMI to rRPMI to dRPMI. At this time point, we observed a significantly reduced cell number in dRPMI medium (Fig. S1, C–F), which could be due to the inability of T cells to proliferate in dRPMI. Thus, even an approximately twofold reduction in $[Mg^{2+}]_i$ in the millimolar range was detrimental to T lymphocyte activation and proliferation.

We subsequently investigated the impact of chronic Mg^{2+} deprivation on TCR signal transduction by culturing T cell blasts in cRPMI, rRPMI, or dRPMI for 96 h and then measuring Ca^{2+} upon TCR engagement. Our assay buffer contains both Ca^{2+} and Mg^{2+} at 1.2 mM each to allow acute fluxes of those ions. Ca^{2+} flux was clearly blunted after TCR stimulation in both CD4$^+$ and CD8$^+$ T cells cultured in dRPMI, but not in rRPMI, as compared with cRPMI (Fig. 1, K and L). Extended incubation in dRPMI also adversely affects cell viability in rapidly proliferating cells (Fig. S1, G and H). Thus, Mg^{2+} deprivation impaired T cell activation, and short-term Mg^{2+} supplementation at the time of stimulation was not sufficient to rescue TCR signaling in cells grown in Mg^{2+}-deprived medium.

We next examined the effect of acute Mg^{2+} deprivation during TCR engagement, which would prevent any transient increase in $[Mg^{2+}]_i$ (Li et al., 2011). To measure immediate TCR responses, we assayed Ca^{2+} fluxes in healthy donor CD4$^+$ and CD8$^+$ T cells in presence or absence of $[Mg^{2+}]_e$. We found that assay buffer with Ca^{2+} only (Ca^{2+}) showed a decreased amplitude of the Ca^{2+} flux in both CD4$^+$ and CD8$^+$ cells compared with buffer with both Ca^{2+} and Mg^{2+} (Ca^{2+}/Mg^{2+}; Fig. 2 A and Fig. S2, A and B). Furthermore, gating on naive (CD45RA$^+$, CCR7$^+$), central memory (CD45RA$^-$, CCR7$^+$), and effector memory (CD45RA$^-$, CCR7$^-$) CD4$^+$ cells revealed a significant reduction in Ca^{2+} fluxes in all three subsets when using assay buffer with no Mg^{2+} (Fig. 2 B). We next performed Western blots to assess the effects on TCR-triggered phosphorylation events with or without Mg^{2+} during TCR engagement. In ex vivo–isolated CD4$^+$ cells stimulated without Mg^{2+}, there was decreased phosphorylation of PLCγ1 (Y783) and SLP76 (Y173) compared with cells stimulated in the presence of both Ca^{2+} and Mg^{2+} (Fig. 2, C and D). TCR activation of the tyrosine kinase IL-2–inducible T cell kinase (ITK) is responsible for both PLCγ1 (Y783) and SLP76 (Y173) phosphorylation (Readinger et al., 2009; Sela et al., 2011). By contrast, ZAP70 and ERK phosphorylation, which does not depend on ITK, was not significantly affected (Fig. 2, C and D). Finally, we evaluated autophosphorylation of ITK on the tyrosine 180 (Y180) site as another measure of ITK activity and found that it was also significantly reduced 3 min after stimulation in the absence of extracellular Mg^{2+} (Fig. 2, E and F), while ERK phosphorylation was only slightly affected (Fig. 2, E and F). This is the step where signal propagation is inhibited in T cells from XMEN patients (Chaigne-Delalande et al., 2013) and is consistent with defects in ITK activity (Fig. S3 A).

ITK catalytic activity is regulated by millimolar changes in $[Mg^{2+}]$

Like all kinases, ITK requires Mg^{2+} as a cofactor at ~30 µM to form the ATP:Mg^{2+} chelate for activity (Bao et al., 2011). However, we hypothesized that there is additional regulation by Mg^{2+} at millimolar concentrations, possibly involving a second, low-affinity binding site. To test this, we measured the effect of varying $[Mg^{2+}]$ on the catalytic activity of purified ITK (Fig. S3 B). Keeping ATP:Mg^{2+} and substrate concentrations constant, we titrated $[Mg^{2+}]$ from 0.1 to 10 mM and observed increased ITK activity following Michaelis–Menten kinetics (Fig. 3 A). The Michaelis constant (K_m) for $[Mg^{2+}]$ was 0.71 mM, predicting that ITK catalytic activity would change markedly at the different $[Mg^{2+}]_i$, as was observed when using Mg^{2+}-deprived or replete conditions (Figs. 1 and 2). The dramatically increased velocity caused by Mg^{2+} in the low-millimolar range indicates a second function for Mg^{2+} in catalysis besides its role as a cofactor for ATP:Mg^{2+}. By comparison, Ca^{2+}, a related alkaline metal cation, and Mn^{2+}, a transition metal often substituted for Mg^{2+}, had no effect on ITK activity. Since BCR signaling closely parallels TCR signaling and there are a number of other tyrosine kinases in both pathways (Fig. S3 C), we tested the effect of $[Mg^{2+}]$ on the activity of Bruton's tyrosine kinase (BTK), the Tec family counterpart of ITK found predominantly in B cells (Kurosaki, 1999; Joseph et al., 2013), lymphocyte-specific protein tyrosine

Kanellopoulou et al.
Mg^{2+} regulation of kinases

Journal of Experimental Medicine
https://doi.org/10.1084/jem.20181970

1829
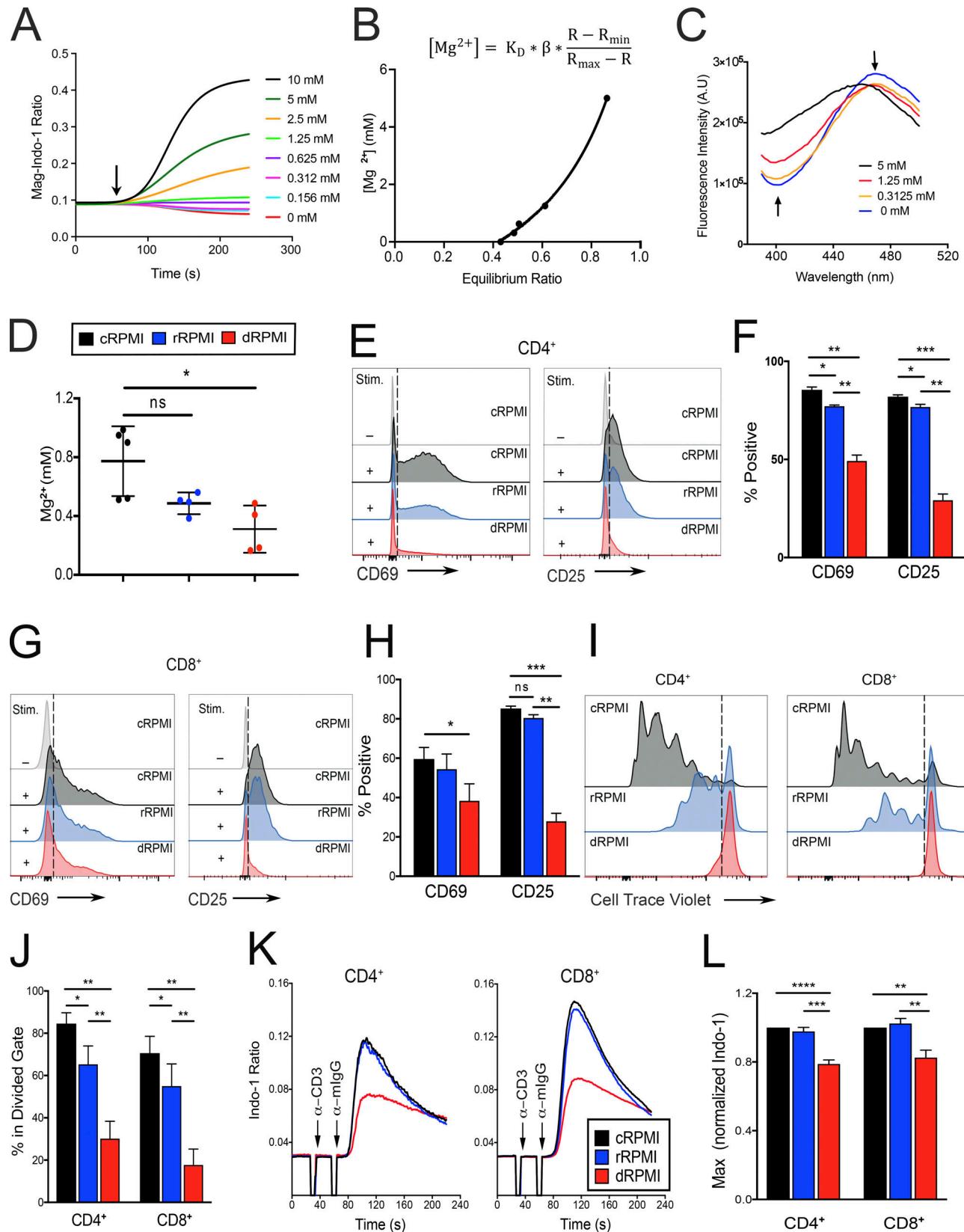
Figure 1. **Defective TCR activation and reduction of basal [Mg²⁺] in T cells deprived of extracellular Mg²⁺. (A)** Representative curve-fitting plot of the flow cytometric Mg²⁺ calibration assay. The y axis shows the ratio of bound to unbound (BUV737/BUV380) Mag-Indo-1 dye. Arrow indicates addition of digitonin. Concentration of extracellular MgSO₄ for each calibration curve is shown on the right. **(B)** Grynkiewicz equation and curve-fitting model used for calculation of [Mg²⁺]ᵢ concentration. K_D, dissociation constant of Mag-Indo-1; β, scaling factor associated with system; R, measured ratio at any given

concentration; R_{max}, ratio at 5 mM Mg^{2+}; R_{min}, ratio at 0 mM Mg^{2+}. **(C)** Plots of fluorescence intensity in A.U. versus wavelength of emission for the fluorometer-based version of the Mg^{2+} calibration assay. Arrows point to the emission wavelengths of the bound and unbound form of the Mag-Indo-1 dye and the direction the peaks shift with increasing Mg^{2+} concentration. **(D)** Quantification of internal Mg^{2+} concentrations in each respective media condition. **(E)** Flow cytometric analysis of CD69 and CD25 expression on $CD4^+$ cells 18 h and 36 h, respectively, after either no stimulation (−) or the addition of 1 µg/ml anti-CD3/CD28 and 1 µg/ml anti-Ig secondary antibody (+) in cRPMI, rRPMI, and dRPMI as indicated. Dashed line indicates the threshold used for positive staining. **(F)** Quantification of the percentage of $CD69^+$ and $CD25^+$ cells shown in E. **(G and H)** Analysis of $CD8^+$ cells as in E and F, respectively. **(I and J)** Flow cytometric analysis of Cell Trace violet fluorescence of labeled $CD4^+$ and $CD8^+$ cells 5 d after anti-CD3/CD28 stimulation in the indicated media; dashed line indicates the threshold used to determine at least one division quantified as percentage in the divided gate (J). **(K)** Flow cytometric analysis of Ca^{2+} flux (plotted as ratio of bound to unbound Indo-1 dye) versus time (s) in $CD4^+$ and $CD8^+$ T cell blasts cultured for 96 h in cRPMI, rRPMI, or dRPMI. Cells were stimulated with 1 µg/ml anti-CD3 and 1 µg/ml anti-Ig secondary antibody as indicated. **(L)** Quantification of the flux observed in K, represented as a fold change of the maximum ratio, based on the maximum obtained in cRPMI. Legend in D indicates experiments done in cRPMI (black), rRPMI (blue), and dRPMI (red). Panels A–C depict a representative replicate of at least three independent experiments. Error bars represent SEM of three (E–I), four (K and L), or five (D) independent experiments. P values were calculated with a paired t test (*, $P < 0.05$; **, $P < 0.01$; ***, $P < 0.001$; ****, $P < 0.0001$; ns, not significant).

kinase (Lck), and ZAP70. All three kinases exhibited an increase in activity, but the effect on initial velocity was less pronounced than for ITK (Fig. S3, D and E; and Table 1). Strikingly, BTK was more active when Mn^{2+} was substituted for Mg^{2+}, indicating that although ITK and BTK are homologous enzymes, their active sites are regulated differently by divalent cations. To verify these results and directly compare ITK and BTK, we purified active FLAG-tagged kinases using a mammalian expression system. These protein preparations also confirmed a dependence on millimolar levels of Mg^{2+} and showed that ITK was less active than BTK, consistent with previous observations (Fig. 3 B; Joseph et al., 2013).

ITK utilizes a second low-affinity Mg^{2+} to configure its catalytic pocket

The variation of ITK enzyme activity with $[Mg^{2+}]$ in the range of 0–2 mM is particularly interesting, because $[Mg^{2+}]_i$ in different types of mammalian cells has been reported to be 0.1–1 mM (Fig. 3 A, right panel; rectangle in Fig. S3, D and E; Buri and McGuigan, 1990; MacDermott, 1990). Thus, ITK could be a "sensor" or rheostat of $[Mg^{2+}]_i$ that controls the physiological response to antigen receptor engagement in T cells with varying $[Mg^{2+}]$ (Li et al., 2011). To understand how millimolar changes in $[Mg^{2+}]_i$ influence ITK activity, we examined the possibility of a second low-affinity Mg^{2+} binding site in its catalytic pocket, which has been reported for cyclin-dependent kinase 2 (CDK2; Sun and Budde, 1997; Shaffer and Adams, 1999; Bao et al., 2011). The available ITK structures do not contain Mg^{2+} ions or ADP/ATP and are typically complexed with chemical inhibitors, so we threaded ITK using I-TASSER (Yang and Zhang, 2015) onto the CDK2 structure containing two Mg^{2+} ions and ADP in the catalytic pocket (Protein Data Bank accession number 3QHW; Bao et al., 2011). We then performed molecular dynamics (MD) modeling with AMBER 16 to evaluate the stabilities and structural effects of these ions on the threaded ITK structure (Case et al., 2017). Like CDK2, ITK can bind two Mg^{2+} ions with appropriate bipyrimidal tetrahedron hexa-coordinate chelation geometry in two distinct hypothetical sites in the catalytic pocket (Fig. 3 C; Bao et al., 2011). By reference to previous convention, the Mg^{2+} ion in the apparent low-affinity, "second" site was designated MgI, and the Mg^{2+} ion in the high-affinity site was designated MgII (Bao et al., 2011; Jacobsen et al., 2012). This model achieved a C score of 1.2, a template modeling score of 0.88 ± 0.07, and a root-mean-square deviation (RMSD) of 3.5 ±

2.4 Å, indicating that it represents a plausible structure that the primary ITK polypeptide chain can adopt (Yang and Zhang, 2015). Several features become apparent when comparing the structures with either one or two Mg^{2+} ions. The ? phosphate of ATP becomes aligned better in the two-Mg^{2+} ion structure with the optimal position for catalysis (shown in gray, with the one Mg^{2+} ion structure on the left; Fig. 3 D). Also, there is a rearrangement of helices and loops lining the active site are now aligned better with the well-characterized "closed" active site structure of CDK2 (Bao et al., 2011). For example, the two-Mg^{2+} ion structure reveals that the glycine-rich loop "clamps" down the roof of the active site, thereby stabilizing the position of the substrate for efficient phosphoryl transfer. We also found that the two-Mg^{2+} conformation has a lower RMSD relative to the transition state conformation, which would contribute to enhanced catalytic activity (Fig. 3 E). In this model, MgII was coordinated sixfold by the oxygens of N487 and D500, the β and gamma phosphate as well as the linking oxygen between them in ATP, and one water (Figs. 3 C and 4 A). In the two-Mg^{2+} structure, MgI formed contacts with a bidentate configuration of the oxygens of the D500 (DFG) carboxylate, the β and γ phosphates, and two water molecules. The distance between Mg^{2+} and the amino acid chelation points were within 2 Å, consistent with the CDK2 structure (Bao et al., 2011; Jacobsen et al., 2012). The steric constraint, previously observed in the CDK2 structure (Bao et al., 2011), was due to chelation by two oxygens from the D500 carboxylate, which have a 60° interoxygen bond angle rather than an ideal equatorial coordination angle of 90° (Fig. 3 C). This nonoptimal coordination, together with the fact that MgI had two chelation sites occupied by water, suggests that its binding is thermodynamically less favorable, thus accounting for the apparent lower affinity of this site compared with the MgII binding site (Bao et al., 2011). By contrast, MgII, which enters the active site as the ATP:Mg^{2+} chelate, has three coordinated oxygens in ATP, only one chelation site occupied by a water molecule, and a more ideal geometry, features that collectively contribute to the apparent higher binding affinity of MgII.

From this analysis, we conjectured that the MgI binding site would be low affinity (K_D [dissociation constant of Mg^{2+} ion] in the millimolar range as opposed to the first site, for which the K_D is in the micromolar range) and strongly affect ITK enzyme activity (Bao et al., 2011). To provide evidence for a second Mg^{2+} affecting catalysis and ensure that the boost in enzyme activity we observed (Fig. 3 A) is not due to the generation of more Mg:
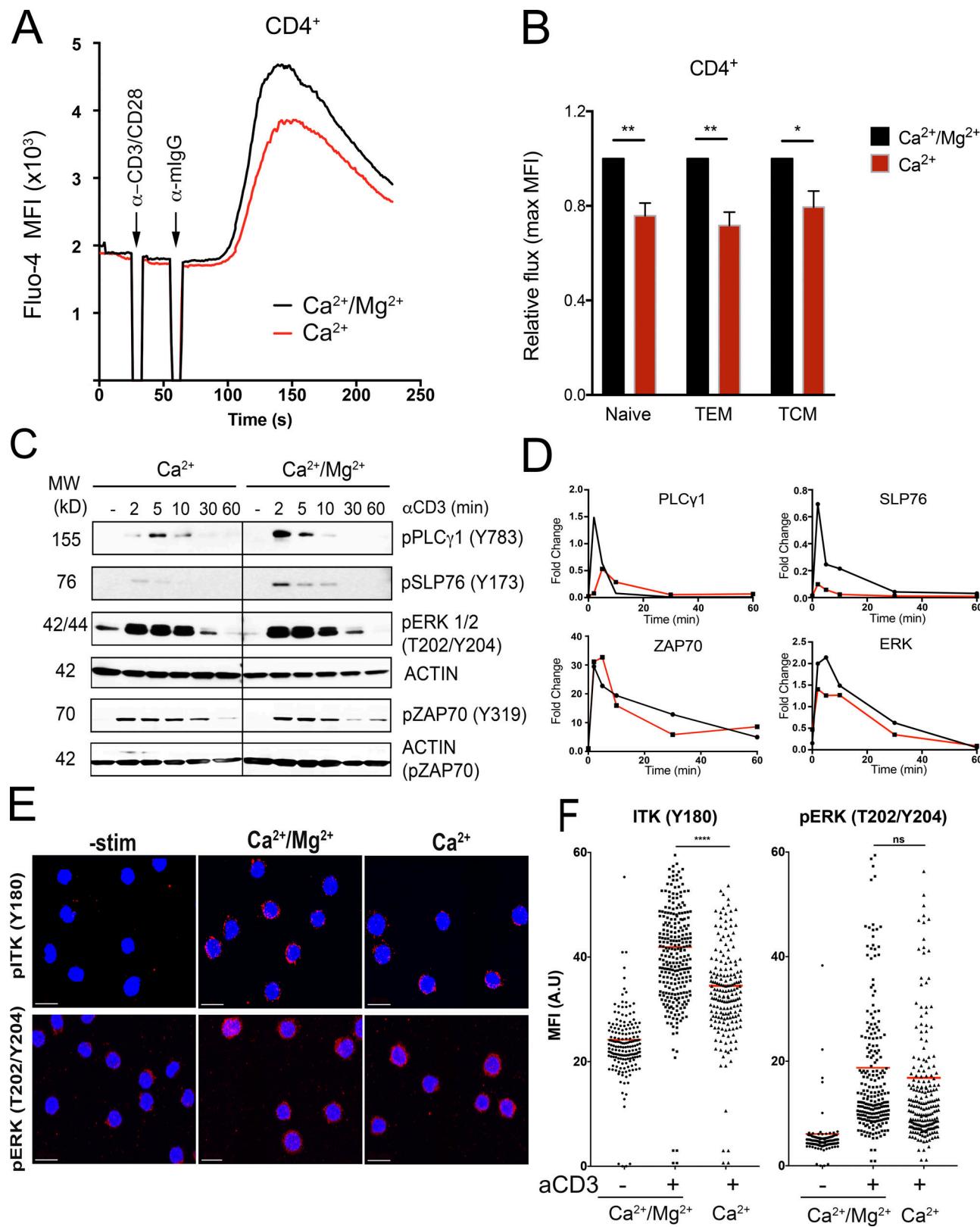
Figure 2. **Acute Mg²⁺ deprivation impairs TCR signaling. (A)** Flow cytometric analysis of Ca²⁺ flux in ex vivo–isolated PBMCs loaded with Fluo-4 and gated on CD4⁺ cells. 1 µg/ml anti-CD3/CD28 and 1 µg/ml anti-Ig secondary antibody was added at the indicated time. Stimulation was performed in buffer containing only 1.2 mM CaCl₂ (Ca²⁺) or 1.2 mM CaCl₂ and 1.2 mM MgSO₄ (Ca²⁺/Mg²⁺). **(B)** Quantification of the peak of the Ca²⁺ flux in different CD4⁺ cells subsets (naive, CD45RA⁺CCR7⁺; central memory T cells [TCM], CD45RA⁻CCR7⁺; and effector memory T cells (TEM), CD45RA⁻CCR7⁻). **(C)** Representative Western blot analysis of phosphorylated proteins as indicated using lysates from ex vivo–isolated CD4⁺ cells stimulated with 10 µg/ml anti-CD3 and 10 µg/ml anti-Ig secondary antibody at the indicated times in buffer containing only 1.2 mM CaCl₂ (Ca²⁺) or 1.2 mM CaCl₂ and 1.2 mM MgSO₄ (Ca²⁺/Mg²⁺). β-Actin is shown as a loading

control. MW, molecular weight. **(D)** Quantification of the signal shown in C from one representative experiment. **(E)** Representative immunofluorescence images of CD4+ cells activated with soluble anti-CD3 and anti-IgG secondary (10 µg/ml each) antibody in different buffers as in C for 3 min and stained with the indicated antibodies. Scale bars represent 10 µM. **(F)** Quantification of the mean fluorescence intensity (MFI) in A.U. using >100 cells/condition for the images in E. Data are the mean of six independent experiments (A and B) or depict a representative replicate of three independent experiments (C–F). Error bars represent SEM. P values were calculated with a paired t test (*, $P < 0.05$; **, $P < 0.01$; ***, $P < 0.001$; ns, not significant).

ATP^{-2}, we used an approach previously described for CDK2 (Jacobsen et al., 2012), in which one measures enzyme activity while titrating pure, Mg^{2+}-free, ATP. Since ATP is a strong chelator for Mg^{2+} ($K_D = 28.6$ µM), it will abstract Mg^{2+} from the second, weak binding site in the enzyme once the [ATP] exceeds that of free Mg^{2+} in the buffer, resulting in inhibition of kinase activity. We titrated ATP at the indicated concentrations while keeping $[Mg^{2+}]_e$ constant at either 2.5 or 5 mM and observed that with increasing ATP, the reaction velocity at low concentrations increased, likely by forming more $Mg:ATP^{-2}$ complex. However, a maximum was reached, and an inhibitory effect was observed at approximately the same concentration as Mg^{2+} included in the reaction (Fig. 4 B). The reduction in activity was not due to removal of the Mg^{2+} from the high-affinity MgII site, since $Mg:ATP^{-2}$ is in excess under these conditions. These data provide evidence Mg^{2+} occupies a second binding site in the enzyme, which is likely the MgI binding site predicted by MD modeling, and that this is necessary for optimal ITK catalytic activity.

Both the N487 and D500 residues, predicted by our modeling to be key Mg^{2+} chelation sites (Fig. 4 A), are highly conserved across tyrosine kinases (TKs; Fig. S4 E; Taylor and Kornev, 2011). The D500 residue in human ITK is part of the canonical DFG loop that regulates kinase activity and contributes two crucial oxygen chelation points in MgI (Taylor and Kornev, 2011). By contrast, N487 is adjacent to MgII and stabilizes the binding of $Mg:ATP^{-2}$ as the enzyme cofactor. We designed mutants that would selectively disrupt only one of the Mg^{2+} chelation points for MgI and MgII, namely N487H and D500N, as well as a previously characterized kinase dead mutant, K390R (Heyeck et al., 1997; Fig. S4, A and B). We expressed and isolated FLAG-tagged mutant ITK proteins together with WT-ITK from mammalian cells (Fig. S4, C and D). To estimate the amount of enzyme needed for the kinase assays, we performed a Western blot for both FLAG and the Lck-mediated activating phosphorylation on Y511 (Fig. S4 D). Since Y511 phosphorylation is required for kinase activity but was not equal across the different proteins, we normalized the input for the kinase assays to the amount of phosphorylated ITK in each preparation to ensure equal amounts of activated enzyme were added to each assay. We observed that WT ITK had significant kinase activity and displayed increased activity when Mg^{2+} was titrated, especially in low-millimolar concentrations, verifying what we observed with the commercially prepared ITK protein (Fig. 3 A). Both mutants, N487H and D500N, predicted to disrupt Mg^{2+} binding to the cofactor site (MgII) or the regulatory site (MgI) abolished enzyme activity as effectively as the kinase-dead, K390R, mutant (Fig. 4 C). Therefore, both Mg^{2+} chelation points and the associated MgI and MgII binding sites are required for ITK phosphotransfer activity.

Augmented activity of other kinases by Mg^{2+}

The signaling cascade downstream of the TCR involves several key TKs besides ITK, including Lck and ZAP70, as well as serine/threonine kinases such as protein kinase C theta (PKCϑ) that are crucial for Ca^{2+} flux or subsequent T cell activation events. Conservation of the N487 and D500 residues (Fig. S4 E) suggested these kinases might also have a low-affinity Mg^{2+} binding site that is important for enzyme activity. As previously mentioned, Lck, ZAP70, and BTK also displayed increased Mg^{2+}-dependent activity. We therefore tested the effects of Mg^{2+} on representative kinases belonging to different families of the kinome. We found that dual-specificity tyrosine-phosphorylation–regulated kinase (DYRK), ERK, PKCϑ, and PKD2 all showed varying degrees of augmented catalytic activity with millimolar increases in $[Mg^{2+}]$ (Fig. 4 D). Using the enzyme kinetic curves, we calculated a K_m for each of these kinases, which we found differed markedly (Fig. 4 E and Table 1). The serine-threonine and dual-specificity kinases, DYRK, ERK, PKCϑ, and PKD2 all exhibited a K_m in the range of 0.2–0.4 mM Mg^{2+} and would be expected to be fully active in T cells at basal Mg^{2+}, which is 0.72 mM (Fig. 4 E and Table 1). ITK had a K_m of 0.71 mM, which would have variable activity reflecting variations in $[Mg^{2+}]_i$ observed under physiological conditions (Fig. 4 E and Table 1). By contrast, BTK, Lck, and ZAP70 had $K_m > 2$ mM and overall higher catalytic activity, indicating their relative insensitivity to perturbations in $[Mg^{2+}]_i$ in the physiological concentration range (Fig. 4 E, Table 1, and Fig.S3, D and E). In conclusion, enzymes essential for lymphocyte activation have a Mg^{2+} dependence within the range that $[Mg^{2+}]_i$ fluctuates, and ITK is the most sensitive to changes near the typical $[Mg^{2+}]_i$ setpoint of 0.7 mM. A generalized model of Mg^{2+}-dependent kinase regulation is illustrated in Fig. 4 F.

Mg^{2+} deprivation in vivo affects viral immunity

We next tested whether changes in serum Mg^{2+} levels can affect immune responses in vivo by restricting dietary Mg^{2+} for ~2 wk before infecting mice intranasally with influenza A virus; lungs and spleen were harvested 8 d after infection (Fig. 5 A). Serum Mg^{2+} levels were monitored, and we observed a ~50% reduction within 1–2 wk. Ca^{2+} levels were not significantly affected (Fig. 5 B). Consistent with the in vitro defects (Fig. 1, E–L; and Fig. 2), we observed a significant reduction in the numbers of both total CD8+ and tetramer+ CD8+ T cells in the lung of Mg^{2+}-deprived mice 8 d after influenza infection (Fig. 5, C, F, and G). CD4+ cells were also reduced (Fig. 5, C–E), albeit to a lower extent. Splenic T cell numbers were not significant between the control and Mg^{2+}-deprived animals (Fig. S5, D–G). We hypothesize that the difference in cell numbers is because Mg^{2+} deprivation affects both the expansion and homing/homeostasis of cells at the site of infection, which might give rise to the difference
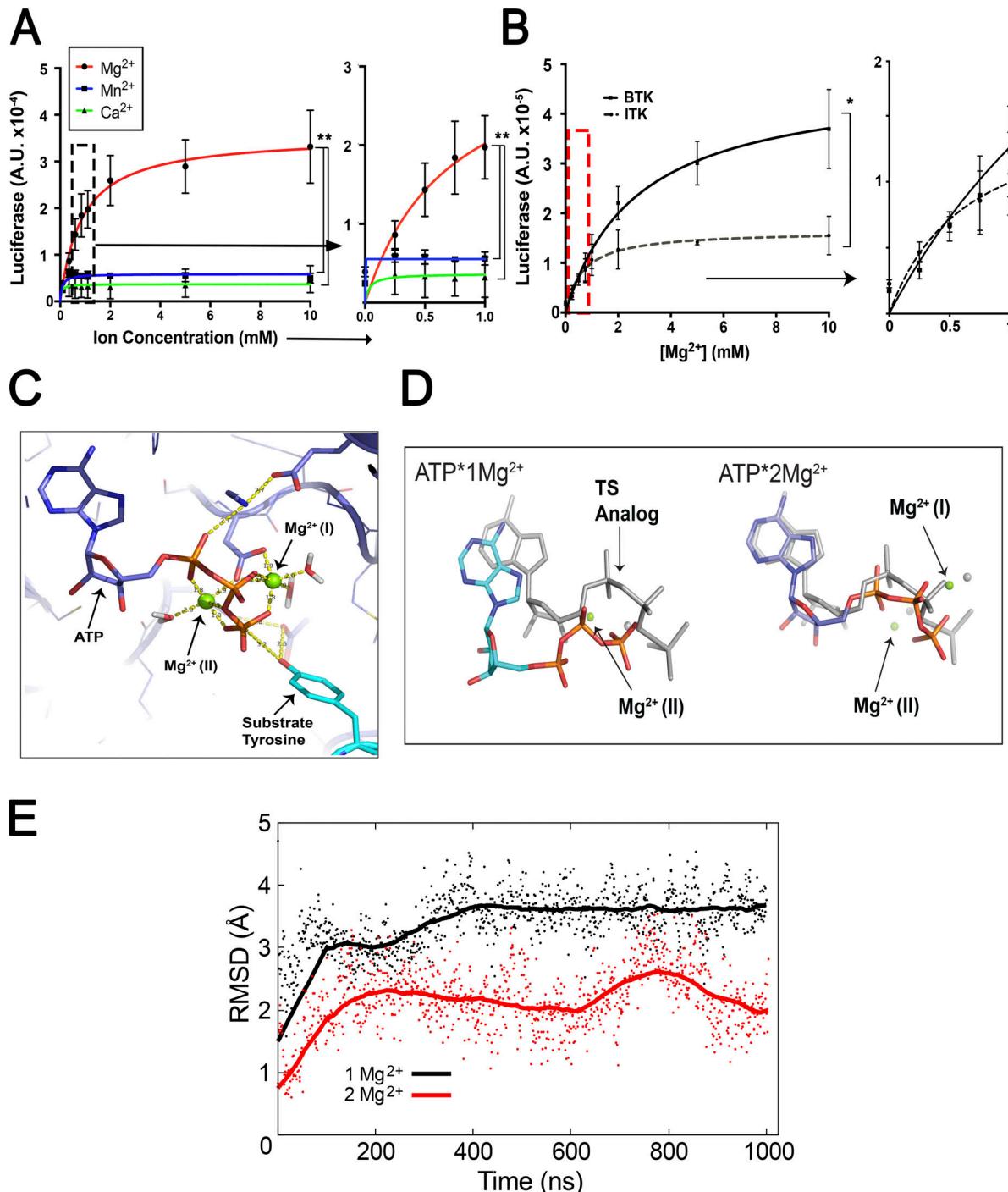
Figure 3. Mg²⁺ can regulate ITK kinase activity at physiological concentrations via two Mg²⁺ binding pockets in the catalytic domain. (A) Kinase activity assay for ITK as a function of increasing MgCl₂ (red), MnCl₂ (blue), and CaCl₂ (green) concentrations. The y axes represent luciferase activity (A.U.). **(B)** Comparison of ITK and BTK kinase activity as a function of [Mg²⁺] using purified FLAG-tagged proteins. Graph to the right shows an expanded axis containing the region boxed by the dashed lines representing the approximate [Mg²⁺]$_i$ measured in lymphocytes (A and B). **(C)** Spatial model of the ITK catalytic pocket complexed with ATP. Mg²⁺ ions are depicted in green. **(D)** MD simulations of ITK with ATP and one Mg²⁺ ion (left) and two Mg²⁺ ions (right) predict that presence of the second Mg ion affects both the orientation and the dynamics of the phosphates. Specifically, the phosphates and Mg²⁺ ion more closely resemble the transition-state mimic conformation (shown in gray) when two Mg²⁺ are bound. Average positions of the ATP and Mg²⁺ ions over the entire trajectory are shown for each 1-μs simulation. Structures were aligned on the protein backbone. The gray ATP and Mg²⁺ reference structures shown are the conformation of the ATP transition-state mimic in CDK2, i.e., ADP/2Mg²⁺/MgF₃⁻ from the Protein Data Bank (3QHW). **(E)** RMSD plot of the position of the γ-phosphate in each simulation relative to the position in the transition state. Points are shown every 1 ns; solid lines are 250-ns rolling average values. Data are the mean of at least three independent experiments or simulations (A–E) ± SEM (A and B). Error bars represent SEM. P values were calculated with a paired t test (*, $P < 0.05$; **, $P < 0.01$).

Table 1. Calculated K_m values for kinases tested in the in vitro activity assay with ion titrations

	K_m [Mg²⁺] mM	K_m [Mn²⁺] mM	K_m [Ca²⁺] mM
ITK	0.71 ± 0.16	0.074 ± 0.04	0.036 ± 0.13
BTK	2.61 ± 0.51	0.333 ± 0.13	0.032 ± 0.1
Lck	2.80 ± 0.26		
ZAP70	2.032 ± 0.54		
ERK1/2	0.374 ± 0.2		
DYRK	0.184 ± 0.05		
PKCθ	0.260 ± 0.07		
PKD2	0.265 ± 0.06		

Calculated K_m values for kinase assays with Mg²⁺, Mn²⁺, and Ca²⁺ for ITK and BTK. Calculated K_m values for kinase assays with Mg²⁺ for LCK, ZAP70, ERK, DYRK, PKCθ, and PKD2.

between the spleen and the lungs. Furthermore, low-Mg²⁺ environments have been demonstrated to induce bronchoconstriction, which could exacerbate the phenotype we see in the Mg²⁺-deprived animals. Consistent with an impaired immune response, viral titers in the lungs of Mg²⁺-deprived mice were significantly higher (Fig. 5 H), and these mice had greater morbidity and lost more weight during infection (Fig. S5 H).

Mg²⁺ deprivation in vivo affects T cell activation

To exclude the possibility that the impaired flu responses we observed in Mg²⁺-deprived mice were due to indirect effects on T cell activation or homing, we tested whether chronic Mg²⁺ deprivation in vivo would recapitulate the T cell activation defects we observed in vitro using Nur77 as a specific T cell activation marker (Ashouri and Weiss, 2017). Mice were deprived of dietary Mg²⁺ for 2 wk, and αCD3 antibody (30 µg, clone 145-2C11) was intravenously injected. Spleens were harvested 2 h after αCD3 injection (Fig. 6 A). Mg²⁺ levels were reduced ∼60% within 2 wk, but Ca²⁺ levels were not significantly affected (Fig. 6 B). Consistent with the in vitro T cell activation defects (Fig. 1, E–L; and Fig. 2), we observed impaired induction of Nur77 in both CD4⁺ and CD8⁺ subsets taken ex vivo in Mg²⁺-deprived samples compared with controls (Fig. 6, C–E). Thus, we conclude that impaired T cell immunity caused by a failure of the Mg²⁺ regulatory mechanisms we have described may be an important component of poor immune responses to influenza in Mg²⁺-deprived mice.

Discussion

Free basal [Mg²⁺]$_i$, which is typically 0.5–1 mM depending on the cell type, can undergo long-term and acute changes with circadian rhythms, cell-surface receptor engagement, or other influences (Whang and Ryder, 1990; Li et al., 2011; Feeney et al., 2016; Uetani et al., 2017). The biological importance of these changes, especially for immune function, and how the cell "senses" them has not been established. We now show that either chronic or acute deprivation of Mg²⁺ decreases the "setpoint" of [Mg²⁺]$_i$ and blocks TCR signal propagation at the level of ITK, which harbors a low-affinity Mg²⁺ binding site that serves as a "sensor" of acute or chronic changes in [Mg²⁺]$_i$ (Madhusudan et al., 2002; Bao et al., 2011; Jacobsen et al., 2012). Although the role of a second Mg²⁺ binding site for enzymes has been debated for years, our study of ITK strongly supports the model of "two metal catalysis" for kinases and shows, for the first time, how this could exert a positive regulatory effect on the physiological activity of a cell, specifically in response to an antigenic stimulus (Bao et al., 2011; Jacobsen et al., 2012). We also note that the K_m that we measured for the second site for other kinases involved in T cell activation, including ERK and PKC, indicates that severe deprivation may begin to impair their function as well lead to multiple roadblocks to full T cell activation.

Low dietary intake causing reduced serum [Mg²⁺] is associated with important chronic health problems, including hypertension, diabetes, metabolic syndrome, kidney disease, and cardiovascular disease (Costello and Nielsen, 2017). With modern food processing and agricultural practices, most people in the United States and the developed world have insufficient dietary intake of Mg²⁺, raising the prospect that Mg²⁺ supplementation or a Mg²⁺-rich diet may improve immune function in otherwise healthy people (Whang and Ryder, 1990; Mayer, 1997; World Health Organization, 2009; Rosanoff et al., 2012; de Baaij et al., 2015). We now show that a reduction in dietary Mg²⁺ can lead to hypomagnesemia and reduced cellular Mg²⁺. The large amount of bound Mg²⁺ in lymphocytes (>10 mM) does not "buffer" the external drop. This has the consequence of impairing T cell activation and compromising the immune response in the lung against inhaled influenza virus infection. Taken together, our work demonstrates how lymphocyte responses are modulated at the molecular level by Mg²⁺ and shows that a Mg²⁺-sufficient diet, which may not be achieved by currently dietary practices in the United States, is crucial for optimal immune function against a common human pathogen.

Materials and methods

Human biospecimens
Healthy control blood was obtained through the National Institutes of Health Clinical Center's blood donor program under approved protocols.

Cell culture and Ca²⁺ flux assays
Peripheral blood mononuclear cells (PBMCs) were isolated from healthy control blood and activated with soluble anti-CD3/CD28 (BioLegend) or CD3/CD28 activation beads (Invitrogen) in cRPMI or dRPMI (USP Biologicals) for 3–4 d as indicated. To expand T cells human recombinant IL-2 (100 U/ml; Roche) was added after 72 h and thereafter, cells were cultured in cRPMI with IL-2. For the ex vivo Ca²⁺ flux experiments, PBMCs were isolated and rested in cRPMI without IL-2 for 24 h before the loading of the dye. Mg²⁺ deprivation was performed on cycling
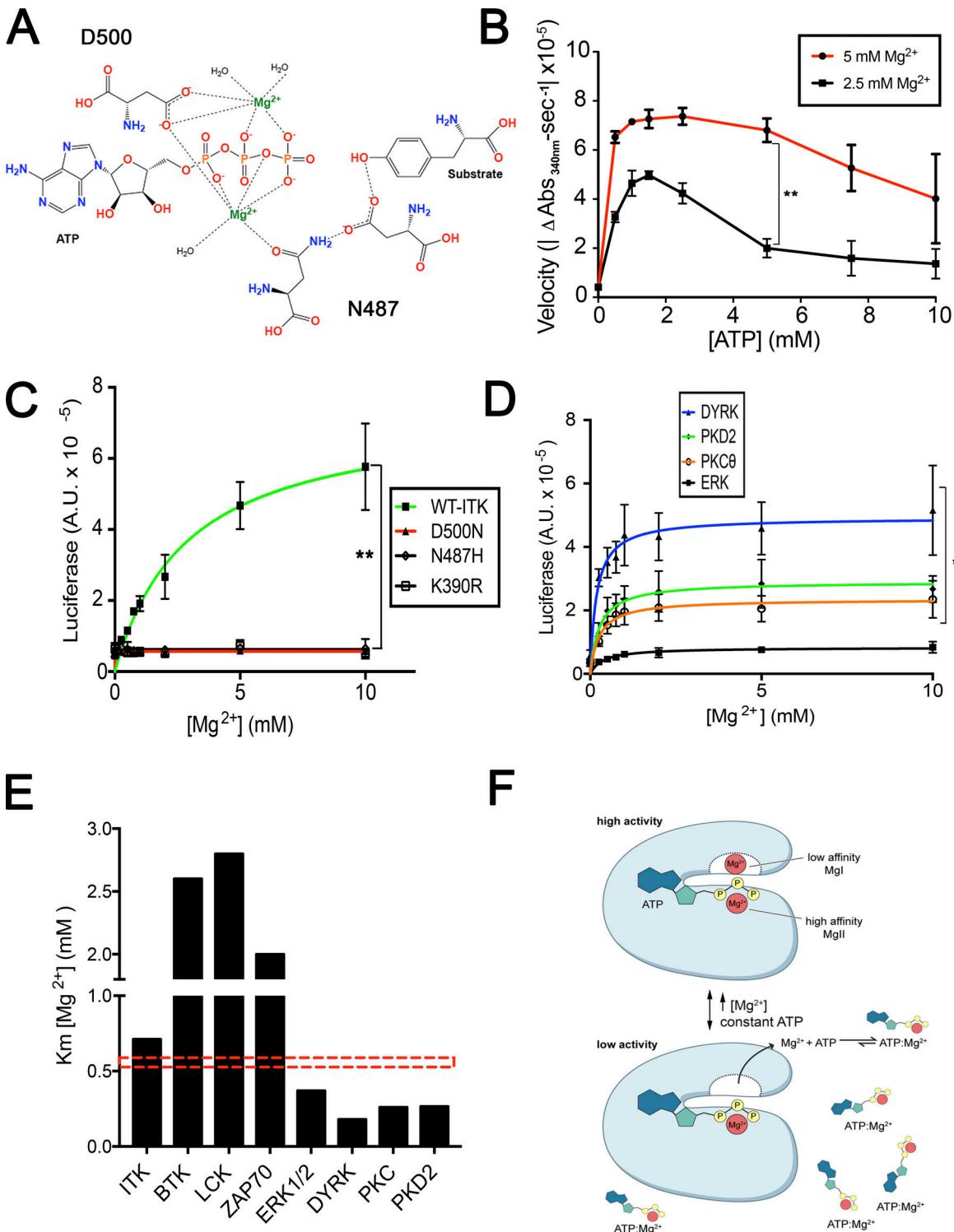
Figure 4. **Regulation of ITK activity is dependent on the low-affinity Mg^{2+} binding site, and mutation of residues that chelate Mg^{2+} in the catalytic pocket of ITK are highly conserved and required for enzymatic activity. (A)** Schematic of the ITK catalytic pocket and the key residues coordinating Mg^{2+} and ATP. **(B)** Pyruvate kinase/lactate dehydrogenase (PK/LDH) assay of ITK titrating ATP at constant Mg^{2+} concentrations (2.5 and 5 mM). **(C)** Kinase assays of in-house–purified full-length ITK (green) and mutants disrupting Mg^{2+} chelation. Catalytically dead K390R ITK was purified as a control. The y axis represents luciferase activity (A.U.). **(D)** Kinase activity assays for DYRK, PKD, ERK, and PKCθ as a function of increasing MgCl$_2$ concentration. **(E)** Bar graph of the average K$_m$ values for Mg^{2+} across different kinases tested in in vitro kinase assays. Red dashed box indicates an approximation of the basal level of [Mg^{2+}]$_i$. **(F)** Provisional model of two site Mg^{2+} regulation for kinases. Data are the mean of three independent experiments ± SEM (B–E). Error bars represent SEM. P values were calculated with a paired t test (*, P < 0.05; **, P < 0.01).
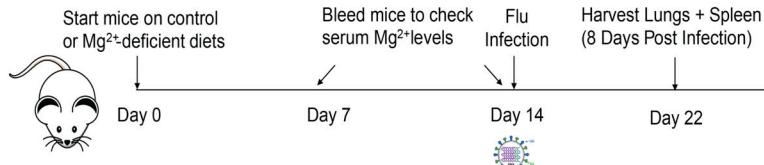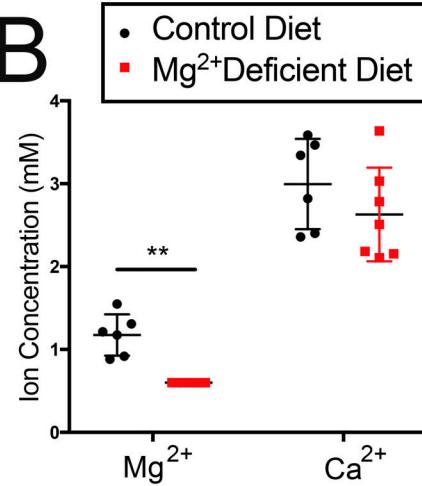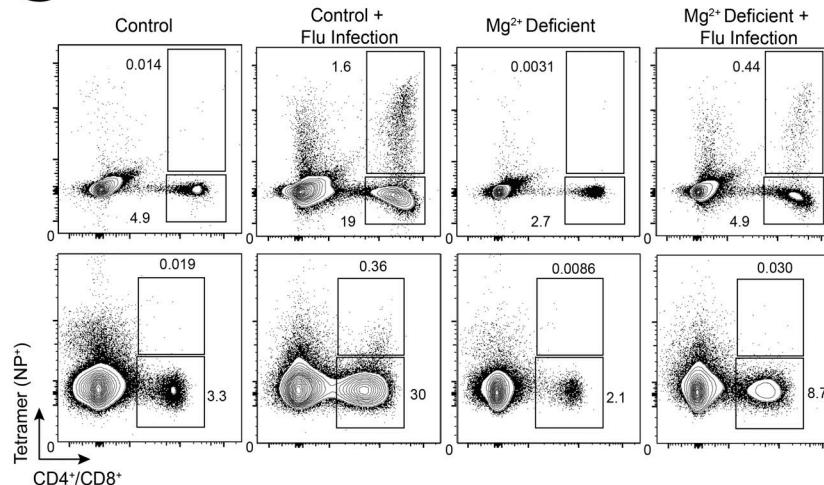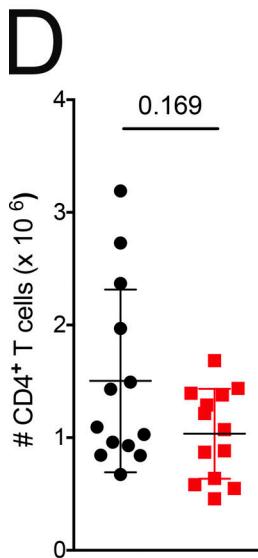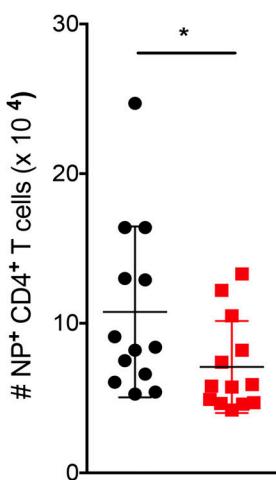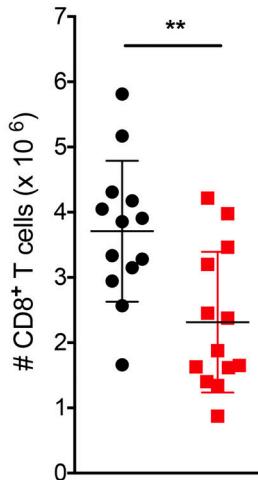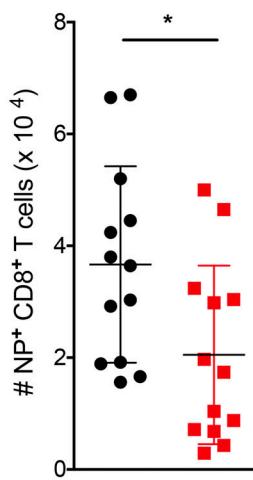
Figure 5. **Mg^{2+} deprivation affects influenza A responses in vivo. (A)** Schematic of the experimental design. **(B)** Mg^{2+} and Ca^{2+} serum levels assayed 13 d after mice (Male C57BL/6) were put on a Mg^{2+}-reduced diet. **(C)** Representative flow cytometric plot of CD4$^+$ and CD8$^+$ cells in lung 8 d after flu infection. **(D–G)** Quantification of the number of CD4$^+$ (D), CD4$^+$NP tetramer$^+$ (E), CD8$^+$ (F), and CD8$^+$ NP tetramer$^+$ (G) cells in lungs of infected mice. **(H)** Quantitative RT-PCR quantification of viral titers from lungs of infected mice. Flu RNA is normalized to Hprt1. Data ± SEM shown are from two (H) or three (D–G) independent experiments with four or five mice in each infected group. Error bars indicate SEM. Panel B depicts a representative replicate of three independent experiments. Legend in B indicates the control diet (black) and the Mg^{2+}-reduced diet (red) for B and D–H. Statistical significance was calculated with a Mann–Whitney *U* test (D–G; *, $P < 0.05$; **, $P < 0.01$) or a paired *t* test (B and H; *, $P < 0.05$; **, $P < 0.01$).
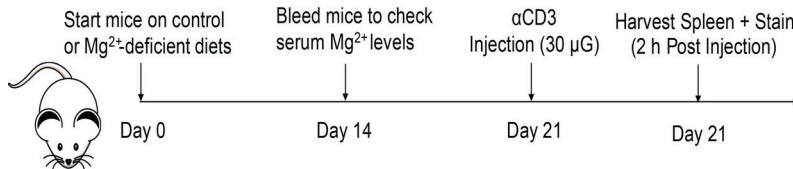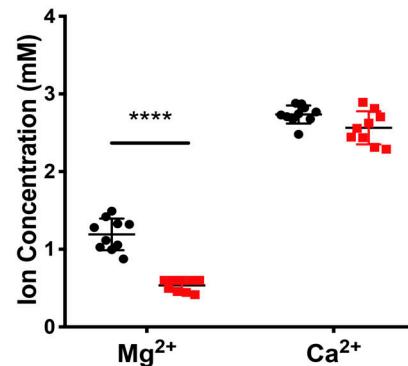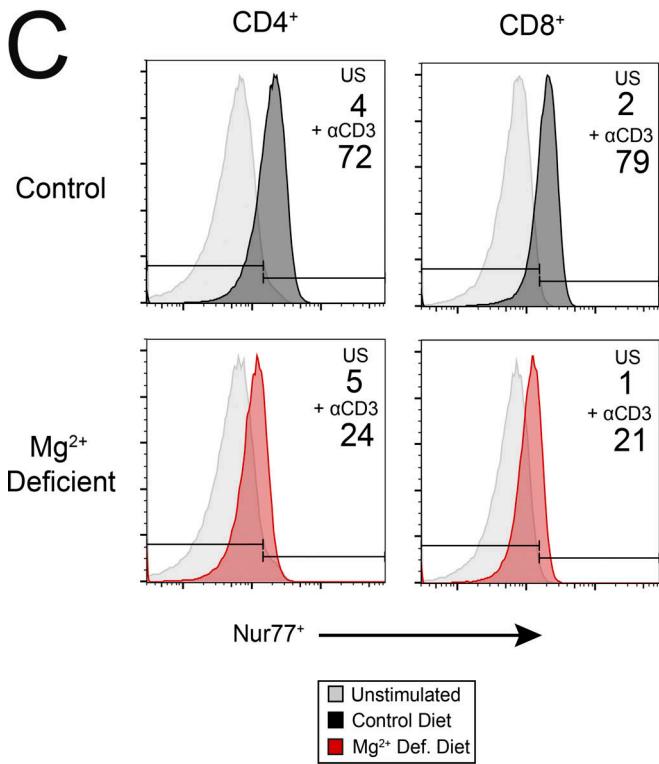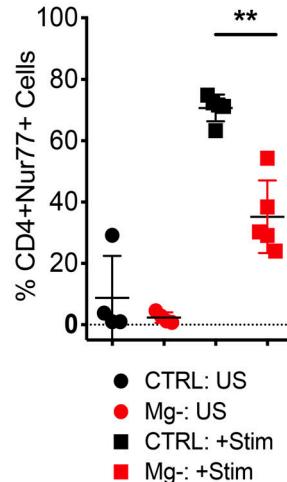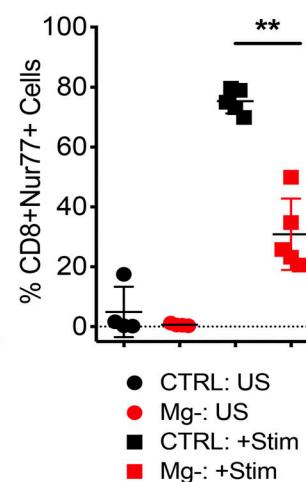
Figure 6. **Mg²⁺ deprivation impairs T cell activation in vivo. (A)** Schematic of the experimental design. **(B)** Mg²⁺ and Ca²⁺ serum levels assayed 14 d after mice (male C57BL/6) were put on a Mg²⁺-reduced diet. **(C)** Representative flow cytometric plot of Nur77⁺ cells in CD4⁺ and CD8⁺ lymphocyte subsets. **(D and E)** Quantification of the number of Nur77⁺CD4⁺ (D) and Nur77⁺CD8⁺ (E) cells in spleens. Unstimulated (US) cells are depicted as circles, while cells stimulated via i.v. α-CD3 injection (Stim) are represented by squares (D and E). Data shown are from three (B and D–E) independent experiments. Error bars represent SEM. P values (****, P < 0.0001) were calculated with a paired t test (B). Panel C depicts a representative replicate of three independent experiments. Plots in D and E represent one or two mice per condition from three independent experiments. Statistical significance was calculated with a Mann–Whitney U test (D and E; *, P < 0.050; **, P < 0.01). CTRL, control.

T cell blasts for 72 h in cRPMI with IL-2 stripped of Mg²⁺ (<0.1 mM) and a Ca²⁺ concentration of 100 mM.

To measure Ca²⁺ flux, cells were loaded with Fluo-4-AM or Indo-1-AM dye (Invitrogen) at a final concentration of 0.5 µM with PowerLoad (Thermo Fisher) in HBSS with 20 mM Hepes (hereby referred to as assay buffer) for 20 min at room temperature (RT). De-esterification of the probe was performed by washing the cells in 1× PBS for 20 min. In the case of the ex vivo Ca²⁺ flux, human Fc block (Invitrogen) was added during de-esterification, and cells were labeled with a-CCR7, a-CD45RA,

aCD4, and aCD8 (BD Biosciences, eBioscience) antibodies in assay buffer. Cells were diluted in buffered HBSS with 1.2 mM Ca²⁺ and Mg²⁺ or 1.2 mM Ca²⁺ 5 min before stimulation. To stimulate cells, anti-CD3 (HIT3a) at 10 µg/ml (BioLegend) and cross-linked with secondary antibody (F′ab₂ fragment goat anti-mouse at 10 µg/ml; Jackson ImmunoResearch) were used. For the ex vivo stimulation, anti-CD28.1 (10 µg/ml; BioLegend) was included with anti-CD3. For all Ca²⁺ flux experiments, events were acquired for 240 s with a BD LSRFortessa or LSR II flow cytometer (BD Biosciences) and analyzed with FlowJo software.

Western blots and immunofluorescence staining for proximal TCR signaling

CD4+ T cells were isolated ex vivo from PBMCs (Stem Cell Technologies). CD4+ cells (12 million) were resuspended (18.5 million cells/ml) in buffered HBSS (650 μl) with 1.2 mM Ca^{2+} and Mg^{2+} or 1.2 mM Ca^{2+} 5 min before stimulation and incubated in a 37°C water bath. 10× radioimmunoprecipitation assay buffer (10 μl) with protease and phosphatase inhibitors (Thermo Fisher) were prepared for each time point (unstimulated and 2, 5, 10, 30, and 60 min) and cells (100 μl) were taken from both buffers for the unstimulated time point, resuspended in radioimmunoprecipitation assay stocks, and then placed on dry ice. Cells were stimulated with anti-CD3 (HIT3a) at 10 μg/ml (BioLegend) and cross-linked with secondary antibody (F'ab₂ fragment goat anti-mouse at 10 μg/ml; Jackson ImmunoResearch). Stimulation time points were obtained using the protocol described for the unstimulated time point. All time-point samples were stored at –80°C. Samples were treated with benzonase nuclease (Sigma-Aldrich) for 40 min at 4°C, diluted 1:1 with SDS loading buffer (Quality Biological), and denatured at 95°C for 20 min. Samples were loaded onto 4–20%Tris-Glycine Gels (Thermo Fisher) and run at 150 V for 1.5 h at RT. Proteins were transferred to a nitrocellulose membrane at 25 V for 1.5 h at RT. Membranes were blocked with 5% milk with 0.1% Tween 20 for 1 h at RT. Membranes were cut and incubated with primary antibodies for p-Plcγ1, p-ZAP70, p-ERK, and p-SLP76 (Cell Signaling Technologies) overnight at 4°C. Samples were washed, incubated with secondary HRP-conjugated anti-rabbit antibody (Cell Signaling Technologies), and washed. Blots were incubated in Luminate Forte Substrate (Millipore) and imaged on a Fuji LAS-3000 system (Fujifilm).

For immunofluorescence staining, ex vivo–isolated CD4+ cells were allowed to adhere to poly-L-lysine–coated coverslips for 10 min. Media was aspirated and replaced with HBSS with 1.2 mM Ca^{2+} or 1.2 mM Ca^{2+}/Mg^{2+} each, and cells were stimulated as described above. At the indicated time after addition of secondary antibody, cells were fixed with 4% paraformaldehyde for 10 min, and ice-cold methanol was added for ≥1 h at –20°C. Coverslips were washed three times with PBS, blocked for 1 h with PBS/0.5% BSA at RT, and incubated with primary antibody in blocking buffer with 0.05% Tween overnight at 4°C. Cells were washed, secondary antibody (anti-rabbit IgG, Alexa Fluor 594; Thermo Fisher) was added for 1 h at RT and washed once in Hoechst 33342 (Thermo Fisher) containing PBS (1 μg/ml). Coverslips were mounted with ProLong Gold Anti-fade reagent (Invitrogen) and imaged with a Leica SP8 microscope.

In vitro kinase assay

All commercial kinase preps were purchased from SignalChem. Kinase activity was measured using the ADP-Glo kinase activity assay by Promega. A custom synthesized peptide substrate (EQEDEPEGIYGVLF) prepared by the National Institute of Allergy and Infectious Diseases Protein Chemistry Section (Bethesda, MD) was kept at a saturating concentration (0.4 mM). Reaction buffers included 50 mM Tris, pH 7.5, 0.1 mg/ml BSA, 1.92 mM DTT, 200 nM ATP, and 4 nM of the respective kinase.

$MgCl_2$ and KCl were added in varying amounts to create the range of free Mg^{2+} titrations (0–10 mM) used in the assay with a final ionic strength of 160 mM (assuming a K_D of 28.6 μM for 1ATP:Mg^{2+}). Reaction mixtures (8 μl total) were prealiquoted in a 384-shallow-well ProxiPlate (PerkinElmer), and kinase was added to initiate catalysis. Following an incubation period of 1 h, the manufacturer's protocol was followed to detect ATP generation. Chemiluminescent intensity of the final luciferase-based reaction was read by an Omega FluoStar Luminometer (BMG LabTech).

Pyruvate kinase and lactate dehydrogenase coupled enzyme assay

All commercial kinase preps were purchased from SignalChem. Kinase activity as a function of time was measured using a coupled enzymatic assay, which measured the production of ADP via the oxidation of NADH to NAD^+ through a pyruvate kinase and lactate dehydrogenase–catalyzed reaction. Reaction buffers (assay buffer) included 100 mM Tris-HCl (pH 7.5), 1.25 mg/ml BSA, 1 mM dithiothreitol, 74 U/ml of pyruvate kinase and lactate dehydrogenase (Sigma-Aldrich), 1 mM phosphoenolpyruvate, 280 μM NADH, and 2.5 mM Mg^{2+} balanced with KCl for a final ionic strength of 0.15 M. Peptide B was kept at a saturating concentration of 0.4 mM. ATP titrations (0–10 mM) were prealiquoted in a half-volume 96-well plate (Corning). Kinase was added (final concentration, 85 nM) to initiate catalysis, and reaction progress was monitored by absorption at 340 nm at RT (25°C) for 2.5 h using a VersaMax Spectrophotometer (Molecular Devices). Data were processed and reaction velocities were calculated using GraphPad Prism v7 and Microsoft Excel 2016.

Null point titration

For the flow cytometric method cycling T cells (12 million cells at 2 million cells/ml) were labeled with Mag-Indo-1-AM dye (Invitrogen) at a final concentration of 0.5 μM with 1× PowerLoad (Thermo Fisher) in assay buffer for 20 min at RT. De-esterification of the probe was performed by washing the cells in 1× PBS for 20 min. The cells were resuspended in HBSS without Ca^{2+} and Mg^{2+} at 34 million cells/ml (~350 μl). Graded concentrations of Mg^{2+} (0, 0.156, 0.312, 0.625, 1.25, 2.5, 5, and 10 mM) were prepared in HBSS (360 μl) without Ca^{2+} and Mg^{2+} assuming a total sample volume of 400 μl. Cells (~1.4 million cells, 40 μl) were added to each Mg^{2+} sample. Cells were acquired for 30 s, permeabilized (add 1.2 μl of 600 μM digitonin), and reacquired on a BD LSRFortessa Flow cytometer (BD Biosciences) for a total of 240 s. Raw data were prepared with FlowJo software. Sigmoidal curve fitting using a modified Hill equation ($R = \frac{\alpha}{\left(\frac{K_A}{I}\right)^n + 1} + \varphi$) was performed using GraphPad Prism v7 with the parameters given in Table S1 to obtain equilibrium ratios for each Mg^{2+} titration point. With these ratios, curve fitting was performed on the plot of $[Mg^{2+}]_{titration}$ versus equilibrium ratio in GraphPad Prism by means of the Grynkiewicz model ($Y = k \times \frac{X - R_{min}}{R_{max} - X}$) and parameters given in Table S2.

The output parameters of this fit (Table S2), $K_D \times \beta$, R_{min}, and R_{max} along with the determination of R (average of the baseline values before the addition of digitonin for the lowest five Mg^{2+}

titrations), were inserted into the Grynkiewicz equation ($[Mg^{2+}] = (K_D \times \beta) \times \frac{R-R_{min}}{R_{max}-R}$) to calculate basal $[Mg^{2+}]$.

For the cuvette method, the same procedure as before was used with the following differences: 30 million cells (2 million cells/ml) were labeled with Mag-Indo-1-AM dye (Invitrogen), and the cells were resuspended in HBSS without Ca^{2+} and Mg^{2+} at 20 million cells/ml (~1,500 µl). 33.3× stock concentrations of Mg^{2+} (for final concentrations of 0, 0.312, 0.625, 1.25, and 5 mM in cuvette) were prepared in HBSS without Ca^{2+} and Mg^{2+} assuming a total sample volume of 120 µl. Cells were added to a UV-compatible quartz microcuvette. Baseline fluorescence emission spectra (390–500 nm) was captured with a fluorometer (Photon Technology International) using an excitation wavelength of 340 nm. Mg^{2+} (3.6 µl of 33.3× stock) from each titration was added followed by 10 µl of 600 µM digitonin (final volume of 120 µl). Subsequent emission spectra were obtained at 1-min intervals following permeabilization with digitonin until the system achieved equilibrium (superimposition of two emission spectra). The baseline ratio is given by the relative intensities at 416 nm and 476 nm of the emission spectra ($R = \frac{I_{416\ nm}}{I_{476\ nm}}$). The equilibrium ratio was calculated using the terminal emission spectra set for each Mg^{2+} titration. With these ratios, curve fitting was performed as previously described.

Molecular modeling
The reference sequence for human ITK was obtained from the UniProt database and was subsequently mapped onto a template crystal structure using the I-TASSER suite. We used a crystal structure of pCDK2 crystallized with two Mg^{2+} ions and an ATP transition-state analogue (Protein Data Bank accession number 3QHW) as our template structure (Jacobsen et al., 2012). We then manually adjusted our model in PyMol (The PyMol Molecular Graphics System, version 1.7.2.1; Schrödinger) such that the side chain angles of residues chelating the catalytic Mg^{2+} ions more accurately resembled the geometry of our pCDK2 template. The one-Mg^{2+} and two-Mg^{2+} bound structures were then immersed in explicit solvent and neutralizing ions, energy minimized, heated, and simulated for length of 1 µs each in AMBER 16. Average structures in Figs. 3 and 4 were generated by superimposing all protein backbone atoms over the trajectory onto the starting structure coordinates.

Protein purification
C-terminal FLAG ITK was cloned into pCDNA3 (Invitrogen) mammalian expression construct. Mutants were generated by site-directed mutagenesis and In Fusion cloning (Clontech). Constructs were transfected in Expi293 cells (Invitrogen) according to the manufacturer's protocol. Cells were harvested 72 h after transfection; before harvesting, cells were treated for 10 min with sodium pervanadate (sodium orthovanadate and hydrogen peroxide; NEB, Calbiochem) to induce protein phosphorylation. Cells were lysed in 150 mM NETN (150 mM NaCl, 0.5 mM EDTA, 20 mM Tris-Cl, pH 8.0, and 0.5% NP-40) buffer, and FLAG-tagged proteins were immunoprecipitated with anti-FLAG-M2 magnetic beads (Sigma-Aldrich). Purified protein was eluted with 3xFLAG peptide (250 µg/ml) in elution buffer (50 mM Tris, pH 8.0, 300 mM NaCl, and 10% glycerol) and stored in elution buffer supplemented to 25% glycerol at –20°C.

Influenza infection
Male C57BL/6 (B6) mice were obtained from The Jackson Laboratory (000664). All mice were maintained under pathogen-free conditions at an American Association for the Accreditation of Laboratory Animal Care accredited animal facility at the National Institute of Allergy and Infectious Diseases and housed in accordance with the procedures outlined in the Guide for the Care and Use of Laboratory Animals under an animal study proposal approved by the National Institute of Allergy and Infectious Diseases Animal Care and Use Committee (LISB 7E). Mg^{2+}-reduced and matching control diets were purchased from Harlan-Teklad. Mouse-adapted influenza A/Puerto Rico/8/1934 H1N1 (influenza PR8) was used for infection (kindly provided by Peter McGuire, National Human Genome Research Institute, Bethesda, MD). Mice (n = 4–5/treatment) were exposed to aerosolized (Glas-Col) 500 PR8 in 10 ml saline. Details of the Mg^{2+} deprivation and infection are outlined in Fig. 5 A. Expression of viral hemagglutinin in the lungs of infected mice was determined by real-time PCR (Tarasenko et al., 2017).

At the indicated times after infection, spleens and lungs were harvested. Single-cell suspensions were prepared from the specified organs and stained for flow cytometry. The lungs were first perfused with PBS and lymphocytes isolated as previously described (Richard et al., 2015).

For MHC class II tetramer staining, cells were incubated with 1 µg/ml NP (311–325, QVYSLIRPNENPAHK) tetramer in cRPMI medium for 1 h at 37°C. For MHC class I tetramer staining, cells were incubated with 0.5 µg/ml NP (366–374, ASNENMETM) tetramer for 30 min on ice. Tetramers were obtained from the National Institutes of Health tetramer core facility.

In vivo αCD3 stimulation
Male C57BL/6 (B6) mice were obtained from The Jackson Laboratory (000664). All mice were maintained under pathogen-free conditions at an American Association for the Accreditation of Laboratory Animal Care accredited animal facility at the National Institute of Allergy and Infectious Diseases and housed in accordance with the procedures outlined in the Guide for the Care and Use of Laboratory Animals under an animal study proposal approved by the National Institute of Allergy and Infectious Diseases Animal Care and Use Committee (LISB 7E). Mg^{2+}-reduced and matching control diets were purchased from Harlan-Teklad. Details of the Mg^{2+} deprivation and αCD3 injection are outlined in Fig. 6 A. Vehicular control (PBS) or 30 µG of αCD3 (2C11 clone) were administered via tail vein injection. Spleens were harvested 2 h after injection. Lymphocytes were fixed in 4% paraformaldehyde and permeabilized overnight in MeOH, and cells were labeled with cells were labeled with aNur77, aCD4, and aCD8 (BD Biosciences, eBioscience) antibodies in assay buffer for 1 h at 4°C. Events were acquired with either a BD LSRFortessa or LSR II flow cytometer (BD Biosciences) and analyzed with FlowJo software.

Online supplemental material

Fig. S1 shows cell viability of cells in media containing different concentrations of Mg^{2+}. Fig. S2 shows that acute Mg deprivation impairs TCR signaling in $CD8^+$ cells. Fig. S3 shows that Mg^{2+} promotes the activity of ITK and other immunologically relevant kinases. Fig. S4 shows purification of ITK mutant proteins. Fig. S5 shows that Mg^{2+} deprivation in mice decreases body weight but does not affect total lung cellularity and splenic T cells. Table S1 lists the parameters and constraints for the modified Hill equation. Table S2 lists the parameters and constraints for the Grynkiewicz model.

References

Ashouri, J.F., and A. Weiss. 2017. Endogenous Nur77 Is a Specific Indicator of Antigen Receptor Signaling in Human T and B Cells. *J. Immunol.* 198: 657–668. https://doi.org/10.4049/jimmunol.1601301

Bao, Z.Q., D.M. Jacobsen, and M.A. Young. 2011. Briefly bound to activate: transient binding of a second catalytic magnesium activates the structure and dynamics of CDK2 kinase for catalysis. *Structure.* 19:675–690. https://doi.org/10.1016/j.str.2011.02.016

Buri, A., and J.A. McGuigan. 1990. Intracellular free magnesium and its regulation, studied in isolated ferret ventricular muscle with ion-selective microelectrodes. *Exp. Physiol.* 75:751–761. https://doi.org/10.1113/expphysiol.1990.sp003457

Case, D.A., T.E. Cheatham, T.A. Darden, R.E. Duke, T.J. Giese, H. Gohlke, A.W. Goetz, D. Greene, N. Homeyer, S. Izadi, et al. 2017. *AMBER 2017.* University of California, San Francisco, CA.

Chaigne-Delalande, B., F.Y. Li, G.M. O'Connor, M.J. Lukacs, P. Jiang, L. Zheng, A. Shatzer, M. Biancalana, S. Pittaluga, H.F. Matthews, et al. 2013. Mg2+ regulates cytotoxic functions of NK and CD8 T cells in chronic EBV infection through NKG2D. *Science.* 341:186–191. https://doi.org/10.1126/science.1240094

Cherepanova, N.A., S. Shrimal, and R. Gilmore. 2014. Oxidoreductase activity is necessary for N-glycosylation of cysteine-proximal acceptor sites in glycoproteins. *J. Cell Biol.* 206:525–539. https://doi.org/10.1083/jcb.201404083

Costello, R.B., and F. Nielsen. 2017. Interpreting magnesium status to enhance clinical care: key indicators. *Curr. Opin. Clin. Nutr. Metab. Care.* 20: 504–511.

Costello, R., T.C. Wallace, and A. Rosanoff. 2016. Magnesium. *Adv. Nutr.* 7: 199–201. https://doi.org/10.3945/an.115.008524

Cundy, T., and J. Mackay. 2011. Proton pump inhibitors and severe hypomagnesaemia. *Curr. Opin. Gastroenterol.* 27:180–185. https://doi.org/10.1097/MOG.0b013e32833ff5d6

de Baaij, J.H.F., J.G.H. Hoenderop, and R.J. Bindels. 2015. Magnesium in man: implications for health and disease. *Physiol. Rev.* 95:1–46. https://doi.org/10.1152/physrev.00012.2014

Deutsch, C., and S.C. Lee. 1988. Cell volume regulation in lymphocytes. *Ren. Physiol. Biochem.* 11:260–276.

Feeney, K.A., L.L. Hansen, M. Putker, C. Olivares-Yañez, J. Day, L.J. Eades, L.F. Larrondo, N.P. Hoyle, J.S. O'Neill, and G. van Ooijen. 2016. Daily magnesium fluxes regulate cellular timekeeping and energy balance. *Nature.* 532:375–379. https://doi.org/10.1038/nature17407

Flatman, P.W., and V.L. Lew. 1980. Magnesium buffering in intact human red blood cells measured using the ionophore A23187. *J. Physiol.* 305:13–30. https://doi.org/10.1113/jphysiol.1980.sp013346

Grynkiewicz, G., M. Poenie, and R.Y. Tsien. 1985. A new generation of Ca2+ indicators with greatly improved fluorescence properties. *J. Biol. Chem.* 260:3440–3450.

Heyeck, S.D., H.M. Wilcox, S.C. Bunnell, and L.J. Berg. 1997. Lck phosphorylates the activation loop tyrosine of the Itk kinase domain and activates Itk kinase activity. *J. Biol. Chem.* 272:25401–25408. https://doi.org/10.1074/jbc.272.40.25401

Jacobsen, D.M., Z.Q. Bao, P. O'Brien, C.L. Brooks III, and M.A. Young. 2012. Price to be paid for two-metal catalysis: magnesium ions that accelerate chemistry unavoidably limit product release from a protein kinase. *J. Am. Chem. Soc.* 134:15357–15370. https://doi.org/10.1021/ja304419t

Joseph, R.E., I. Kleino, T.E. Wales, Q. Xie, D.B. Fulton, J.R. Engen, L.J. Berg, and A.H. Andreotti. 2013. Activation loop dynamics determine the different catalytic efficiencies of B cell- and T cell-specific tec kinases. *Sci. Signal.* 6:ra76. https://doi.org/10.1126/scisignal.2004298

Kurosaki, T. 1999. Genetic analysis of B cell antigen receptor signaling. *Annu. Rev. Immunol.* 17:555–592. https://doi.org/10.1146/annurev.immunol.17.1.555

Li, F.Y., B. Chaigne-Delalande, C. Kanellopoulou, J.C. Davis, H.F. Matthews, D.C. Douek, J.I. Cohen, G. Uzel, H.C. Su, and M.J. Lenardo. 2011. Second messenger role for Mg2+ revealed by human T-cell immunodeficiency. *Nature.* 475:471–476. https://doi.org/10.1038/nature10246

MacDermott, M. 1990. The intracellular concentration of free magnesium in extensor digitorum longus muscles of the rat. *Exp. Physiol.* 75:763–769. https://doi.org/10.1113/expphysiol.1990.sp003458

Madhusudan, P., P. Akamine, N.H. Xuong, and S.S. Taylor. 2002. Crystal structure of a transition state mimic of the catalytic subunit of cAMP-dependent protein kinase. *Nat. Struct. Biol.* 9:273–277. https://doi.org/10.1038/nsb780

Mayer, A.-M. 1997. Historical changes in the mineral content of fruits and vegetables. *Br. Food J.* 99:207–211. https://doi.org/10.1108/00070709710181540

Meyer, T.E., G.C. Verwoert, S.J. Hwang, N.L. Glazer, A.V. Smith, F.J. van Rooij, G.B. Ehret, E. Boerwinkle, J.F. Felix, T.S. Leak, et al. Meta Analysis of Glucose and Insulin Related Traits Consortium. 2010. Genome-wide association studies of serum magnesium, potassium, and sodium concentrations identify six Loci influencing serum magnesium levels. *PLoS Genet.* 6:e1001045. https://doi.org/10.1371/journal.pgen.1001045

Ng, L.L., J.E. Davies, and M.C. Garrido. 1991. Intracellular free magnesium in human lymphocytes and the response to lectins. *Clin. Sci. (Lond.).* 80:539–547. https://doi.org/10.1042/cs0800539

Readinger, J.A., K.L. Mueller, A.M. Venegas, R. Horai, and P.L. Schwartzberg. 2009. Tec kinases regulate T-lymphocyte development and function: new insights into the roles of Itk and Rlk/Txk. *Immunol. Rev.* 228:93–114. https://doi.org/10.1111/j.1600-065X.2008.00757.x

Richard, A.C., C. Tan, E.T. Hawley, J. Gomez-Rodriguez, R. Goswami, X.P. Yang, A.C. Cruz, P. Penumetcha, E.T. Hayes, M. Pelletier, et al. 2015. The TNF-family ligand TL1A and its receptor DR3 promote T cell-mediated allergic immunopathology by enhancing differentiation and pathogenicity of IL-9-producing T cells. *J. Immunol.* 194:3567–3582. https://doi.org/10.4049/jimmunol.1401220

Rosanoff, A., C.M. Weaver, and R.K. Rude. 2012. Suboptimal magnesium status in the United States: are the health consequences underestimated? *Nutr. Rev.* 70:153–164. https://doi.org/10.1111/j.1753-4887.2011.00465.x

Sela, M., Y. Bogin, D. Beach, T. Oellerich, J. Lehne, J.E. Smith-Garvin, M. Okumura, E. Starosvetsky, R. Kosoff, E. Libman, et al. 2011. Sequential phosphorylation of SLP-76 at tyrosine 173 is required for activation of T and mast cells. *EMBO J.* 30:3160–3172. https://doi.org/10.1038/emboj.2011.213

Shaffer, J., and J.A. Adams. 1999. Detection of conformational changes along the kinetic pathway of protein kinase A using a catalytic trapping technique. *Biochemistry.* 38:12072–12079. https://doi.org/10.1021/bi991109q

Shrimal, S., N.A. Cherepanova, and R. Gilmore. 2015. Cotranslational and posttranslocational N-glycosylation of proteins in the endoplasmic reticulum. *Semin. Cell Dev. Biol.* 41:71–78. https://doi.org/10.1016/j.semcdb.2014.11.005

Sun, G., and R.J. Budde. 1997. Requirement for an additional divalent metal cation to activate protein tyrosine kinases. *Biochemistry.* 36:2139–2146. https://doi.org/10.1021/bi962291n

Tarasenko, T.N., S.E. Pacheco, M.K. Koenig, J. Gomez-Rodriguez, S.M. Kapnick, F. Diaz, P.M. Zerfas, E. Barca, J. Sudderth, R.J. DeBerardinis, et al. 2017. Cytochrome c Oxidase Activity Is a Metabolic Checkpoint that Regulates Cell Fate Decisions During T Cell Activation and Differentiation. *Cell Metab.* 25:1254–1268.e7. https://doi.org/10.1016/j.cmet.2017.05.007

Taylor, S.S., and A.P. Kornev. 2011. Protein kinases: evolution of dynamic regulatory proteins. *Trends Biochem. Sci.* 36:65–77. https://doi.org/10.1016/j.tibs.2010.09.006

Tong, G.M., and R.K. Rude. 2005. Magnesium deficiency in critical illness. *J. Intensive Care Med.* 20:3–17. https://doi.org/10.1177/0885066604271539

Uetani, N., S. Hardy, S.P. Gravel, S. Kiessling, A. Pietrobon, N.N. Wong, V. Chénard, N. Cermakian, J. St-Pierre, and M.L. Tremblay. 2017. PRL2 links magnesium flux and sex-dependent circadian metabolic rhythms. *JCI Insight.* 2:e91722. https://doi.org/10.1172/jci.insight.91722

Weston, J. 2008. Biochemistry of magnesium. *In The Chemistry of Organo-magnesium Compounds.* John Wiley & Sons, Ltd., Hoboken, NJ. pp. 315–367. https://doi.org/10.1002/9780470751879.ch8

Whang, R., and K.W. Ryder. 1990. Frequency of hypomagnesemia and hypermagnesemia. Requested vs routine. *JAMA.* 263:3063–3064. https://doi.org/10.1001/jama.1990.03440220087036

World Health Organization. 2009. Calcium and Magnesium in Drinking Water. Available at: https://www.who.int/water_sanitation_health/publications/publication_9789241563550/en/ (accessed March 22, 2019).

Yang, J., and Y. Zhang. 2015. I-TASSER server: new development for protein structure and function predictions. *Nucleic Acids Res.* 43(W1):W174-81. https://doi.org/10.1093/nar/gkv342

Zhou, H., and D.E. Clapham. 2009. Mammalian MagT1 and TUSC3 are required for cellular magnesium uptake and vertebrate embryonic development. *Proc. Natl. Acad. Sci. USA.* 106:15750–15755. https://doi.org/10.1073/pnas.0908332106